AGU PUBLICATIONS

JGR

Journal of Geophysical Research: Planets

RESEARCH ARTICLE

10.1002/2014JE004746

Key Points:
- Impact cratering produces characteristic variations in the topographic PSD
- The size-frequency distribution and shape of craters control PSD variations
- We investigate the topographic PSD on model terrains and lunar topography

Correspondence to:
M. A. Rosenburg,
megr@gps.caltech.edu

Citation:
Rosenburg, M. A., O. Aharonson, and R. Sari (2015), Topographic power spectra of cratered terrains: Theory and application to the Moon, *J. Geophys. Res. Planets*, *120*, 177–194, doi:10.1002/2014JE004746.

Received 21 OCT 2014
Accepted 9 JAN 2015
Accepted article online 12 JAN 2015
Published online 13 FEB 2015

Topographic power spectra of cratered terrains: Theory and application to the Moon

Margaret A. Rosenburg[1], Oded Aharonson[2], and Re'em Sari[3]

[1]Division of Geological and Planetary Sciences, California Institute of Technology, Pasadena, California, USA, [2]Department of Earth and Planetary Sciences, Weizmann Institute of Technology, Rehovot, Israel, [3]Racah Institute of Physics, Hebrew University of Jerusalem, Jerusalem, Israel

Abstract Impact cratering produces characteristic variations in the topographic power spectral density (PSD) of cratered terrains, which are controlled by the size-frequency distribution of craters and the spectral content (shape) of individual features. These variations are investigated here in two parallel approaches. First, a cratered terrain model, based on Monte Carlo emplacement of craters and benchmarked by an analytical formulation of the one-dimensional PSD, is employed to generate topographic surfaces at a range of size-frequency power law exponents and shape dependencies. For self-similar craters, the slope of the PSD, β, varies inversely with that of the production function, α, leveling off to 0 at high α (surface topography dominated by the smallest craters) and maintaining a roughly constant value ($\beta \sim 2$) at low α (surface topography dominated by the largest craters). The effects of size-dependent shape parameters and various crater emplacement rules are also considered. Second, we compare the model-derived predictions for the behavior of the PSD with values of β calculated along transects from the Lunar Orbiter Laser Altimeter (LOLA). At small scales (~115 m to 1 km) model predictions agree well with the PSD slope over the observed range of lunar size-frequency distributions. Differences between global PSD slopes at subkilometer and kilometer scales reflect a scale separation in roughness consistent with prior observations using a variety of surface roughness parameters. Understanding the statistical markers left by the impact cratering process on the lunar surface is useful for distinguishing between competing geological processes on planetary surfaces throughout the solar system.

1. Introduction

The high resolution of the topography data set recently recorded by the Lunar Laser Orbiter Altimeter (LOLA), together with ongoing improvements in computing power, provides unprecedented opportunities to correlate model results with observed lunar features. Nowhere is this more pertinent than in impact crater studies. The evolution of cratered terrains is not well understood, despite decades of study [*Melosh*, 1989; *Richardson et al.*, 2005; *Richardson*, 2009], but our understanding of it is crucial to our knowledge of planetary bodies, especially those for which nonphotographic data are scarce, such as the outer planet satellites. Numerical cratering models have seen vast improvements in spatial resolution over the past two decades [*Richardson*, 2009; *Howard*, 2007] and are now capable of tackling a range of crater scales broad enough to allow comparison with real cratered terrains. At the same time, renewed efforts to map the Moon down to meter scales have been stimulated by the abundance of high-resolution images returned by the Lunar Reconnaissance Orbiter Camera (LROC), including recent citizen scientist projects to count craters and evaluate counting statistics [*Robbins et al.*, 2014].

A quantitative comparison of cratered terrain model results and lunar topography analysis thus has never been more feasible, on hand, and relevant to further our understanding of lunar surface processes. To this end, we have developed a cratered terrain model that generates surfaces saturated with craters and have used it to investigate the statistical properties of such landscapes and how they depend on factors such as the size-frequency distribution of impactors, crater shape, and competing surface processes. By keeping track of topography as craters accumulate, the model allows us to evaluate the power spectral density (PSD) before and after the surface has attained equilibrium. Finally, comparing our results to the lunar topography, in both highland and mare regions, can help to distinguish among markers of competing geomorphologic processes acting on the lunar surface.

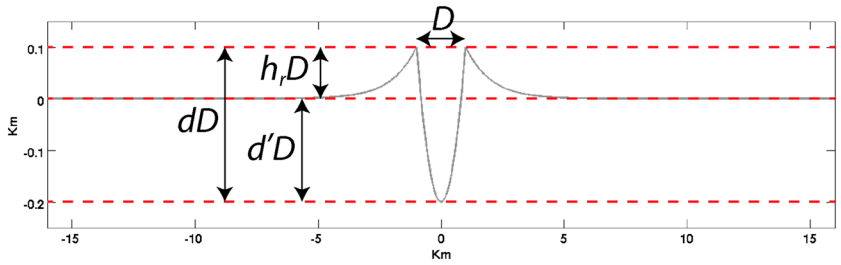

Figure 1. Crater shape parameters used in the numerical and analytic models. The measurable quantity (rim-to-floor) depth-to-diameter ratio (d) is given by $d = d' + h_r$, the depth below the surrounding terrain and the rim height, respectively (both normalized by diameter). The exponential shape of the ejecta blanket is controlled by the ejecta falloff exponent, γ.

2. Models

Any impact cratering model necessarily simplifies a set of complex, local, and interdependent processes, many of which remain active areas of research in their own right. Depending on the task at hand, different researchers have chosen to model different aspects of the cratering process, from a highly detailed slope-failure and regolith-tracking approach [*Richardson*, 2009] to a landscape generator used to study aeolian and fluvial systems on Mars [*Howard*, 2007]. Whatever the goal, two primary phases of crater emplacement must be observed: (1) some degree of erasure, or resetting, of the initial topography and (2) superposition of the crater shape. Here we study the characteristic statistical properties of cratered terrains in order to more easily identify and disentangle signatures of competing geomorphologic processes on planetary surfaces. Modeling is divided into three phases. First, we develop a one-dimensional Monte Carlo simulation that emplaces craters on a flat domain with periodic boundary conditions. Resetting is accomplished through a simple rule: once the location for a new crater has been selected, the existing topography is surveyed and the area within the crater rim is reset to its own mean. In the second modeling phase, we use an analytic formulation to benchmark the 1-D numerical model for terrains accumulating craters of a single size. We then develop a procedure for combining craters of different sizes according to a given size-frequency distribution. The resulting synthetic power spectral density can be directly compared to that generated using the 1-D emplacement model. This analytical formulation is valuable as a point of comparison for the numerical simulations, and it provides a framework to interpret the results. Using the numerical and analytic models together, we can thus understand the evolution of 1-D cratered terrains, starting from a flat profile and proceeding to equilibrium. Finally, we move to a two-dimensional domain and compute the power spectral density along 1-D transects to allow for direct comparison to the LOLA topography data set.

2.1. One-Dimensional Numerical Model

One-dimensional craters consisting of a cavity and an exponentially decaying ejecta blanket are accumulated on a flat domain of size X with periodic boundary conditions. Crater shape is parameterized by depth-to-diameter ratio, d (referring to the rim-to-floor depth), rim height-to-diameter ratio, h_r, and exponential ejecta falloff exponent, γ. For all 1-D models, a parabolic cavity shape is adopted, yielding the following crater shape equation:

$$h(x) = \begin{cases} \left(d' + h_r\right) D \left(\frac{2x}{D}\right)^2 - d'D & |x| \le \frac{D}{2} \\ h_r D e^{\gamma\left(1 - \left|\frac{2x}{D}\right|\right)} & |x| > \frac{D}{2}, \end{cases} \tag{1}$$

where d' is the depth below the surrounding terrain $\left(d' = d - h_r\right)$ normalized by the crater diameter (see Figure 1). For 1-D volume-conserving craters, the three parameters d, h_r, and γ are not independent variables but are related by the expression:

$$\gamma = \frac{3h_r}{2d' - h_r} \tag{2}$$

when $m = 2$, as derived from simple geometry.

We first consider self-similar crater shapes, and subsequently introduce more realistic, size-dependent shape parameters. Crater diameters are chosen according to a specified size-frequency distribution characterized by the power law exponent α:

$$N_c \propto \left(\frac{D}{D_0}\right)^{-\alpha}, \tag{3}$$

where N_c is the cumulative size-frequency distribution (in units of number of craters per unit area) and D_0 is a reference size.

Crater locations are selected at random, and the initially flat plane (or profile, in the 1-D case) accumulates enough craters to completely cover the surface several times. Equilibrium, defined here as the point at which the PSD ceases to change with the addition of more craters, is achieved first at the highest frequency and evolves to lower frequency as larger craters are emplaced. Once equilibrium has been achieved for the scales corresponding to the frequency range of interest, the PSD is computed and averaged over time to provide the best estimate of the equilibrium power spectral density.

$$P(k) = \frac{1}{X}\left[\int_{-X/2}^{X/2} e^{-ikx} h(x)\mathrm{d}x\right]^2. \tag{4}$$

We use two methods to compute the PSD. First, we use fast Fourier transform, from which the PSD can be directly computed from the square of the coefficients, as in equation (4). Second, we employ a multitaper method to estimate the power spectral density with several filters (implemented by MATLAB's function `pmtm`). This is a useful tool for analyzing nonperiodic signals like the lunar topography data collected by LOLA. Both the direct (fast Fourier transform, FFT) method and the multitaper approach provide robust estimates of the PSD for our model, but only the latter is used in our comparison of the model results to the lunar data.

To a first approximation, craters of diameter D are topographic features with a characteristic height, $H(D)$. These features, placed at random, contribute to the overall topography in a manner similar to a random walk, in that they can add coherently or incoherently, and the elevations they build therefore increase roughly as the square root of the number emplaced. The exponential term of the Fourier integral (equation (4)) is approximately constant over a scale D (i.e., for values of $k \leq 1/D$, the term e^{-ikx} is approximately constant relative to the topography added by new craters). The number of these craters contributing to the power is $f_D X/D$ (for the 1-D case), where f_D is the fraction of the domain covered by craters of this size. Equation (4) can thus be rewritten as

$$P(k) = \frac{1}{X}\left[\int_0^X e^{-ikx} h(x)\mathrm{d}x\right]^2 \sim \frac{1}{X}\left[H(D)D\sqrt{\frac{f_D X}{D}}\right]^2. \tag{5}$$

For our model craters, the amplitude H can be thought of as the rim-to-floor depth, $H = \mathrm{d}D$. More rigorously, the equilibrium power spectral density of a surface saturated with craters of a single size D can be calculated analytically by considering the two phases of crater emplacement specified in the numerical model: (1) resetting of initial topography and (2) building of the crater shape. The latter procedure is straightforward, as the superposition of the crater shape on the newly reset topography translates to a linear addition of power in the frequency domain. The power spectral density of our crater shape function (equation (1)) can be written by evaluating equation (1) with equation (4):

$$P_{\mathrm{build}} = \frac{2}{X}\left[\frac{D}{2}\left(\frac{4h_r}{k}\sin\frac{kD}{2} + \frac{16\left(d' + h_r\right)}{k^2 D}\cos\frac{kD}{2} - \frac{32\left(d' + h_r\right)}{k^3 D^2}\sin\frac{kD}{2}\right) + \frac{2h_r D^2\left(2\gamma\cos\frac{kD}{2} - kD\sin\frac{kD}{2}\right)}{4\gamma^2 + (kD)^2}\right]^2. \tag{6}$$

The crater shape PSD depends strongly on the ratio of rim height to crater depth, which through equation (2) also controls the lateral extent of the ejecta blanket. Craters with no ejecta must have unrealistically tall rims to remain volume conserving $\left(h_r = 2d'\right)$. These craters contribute most of their power to wavelengths on the order of their diameter D. As the ratio h_r/d' decreases, the peak of the crater shape PSD broadens and moves to longer wavelengths, as the spatial footprint of the crater increases

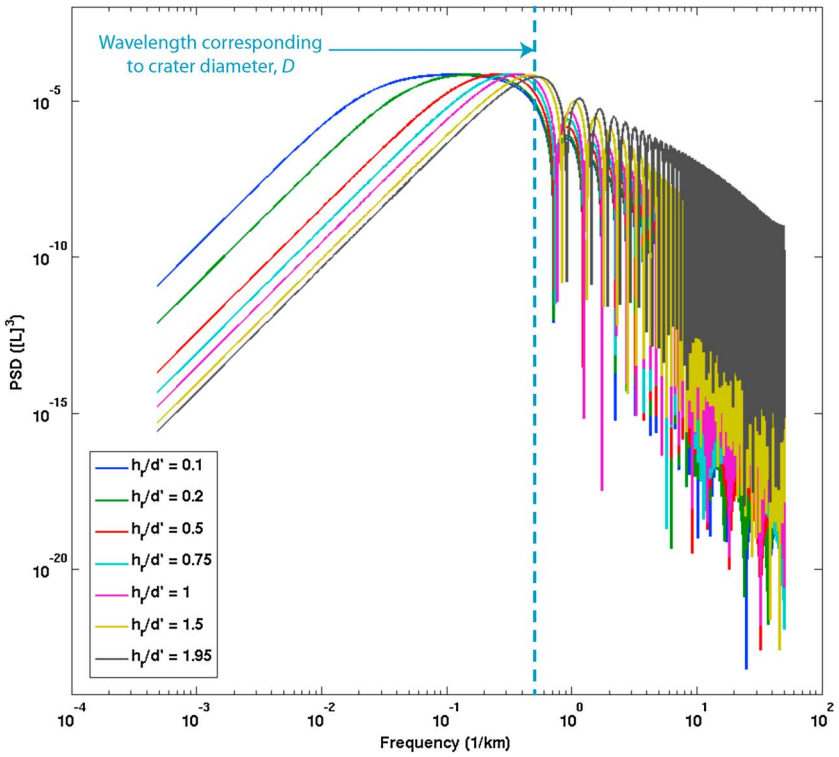

Figure 2. Examples of crater shape PSDs (P_{build}) for craters with diameter $D=2$ km. For volume-conserving craters, the ratio h_r/d' determines the value of the ejecta falloff exponent, γ, which in turn controls the shape of the crater shape PSD. Craters with no ejecta blanket ($h_r/d=2, \gamma=\infty$) have a narrow peak at frequency $f=1/D(k=2\pi/D)$. For $h_r/d'<2$, the peak in the PSD broadens and shifts to lower frequencies as the footprint of the crater increases. Peaks at high frequencies occur at wavelengths corresponding to multiples of the crater footprint.

(Figure 2). For self-similar craters, the peak frequency of the crater shape PSD is inversely proportional to D and the peak power scales as D^4, regardless of the crater shape parameters chosen.

To find an analytical expression to represent the resetting of initial topography, we first consider a harmonic surface with power in a single arbitrary frequency, k^*, over a domain X, within which an area D is reset to its own mean:

$$h(x)=\begin{cases}\cos k^*x & |x-x_c|\le\frac{D}{2}\\ \frac{1}{D}\int_{x_c-D/2}^{x_c+D/2}\cos k^*x\mathrm{d}x & |x-x_c|>\frac{D}{2},\end{cases} \tag{7}$$

where x_c is the center of the new crater and the region to be reset. Considering that the reset region can fall anywhere within the domain X, we must also average over all possible crater locations, and we can write an equation for the Fourier Transform of this function as follows:

$$F_{reset}=\int_{-X/2}^{X/2}\cos k^*xe^{-ikx}\mathrm{d}x+\int_{x_c-D/2}^{x_c+D/2}\left(\frac{2}{k^*D}\sin\frac{k^*D}{2}\cos k^*x_c-cosk^*x\right)e^{-ikx}\mathrm{d}x. \tag{8}$$

In calculating the PSD from this function, we find that the first term yields a Kronecker Delta function with height X^2 at $k=k^*$, while the second term integrates to a function that increases as k^2 at small frequencies, peaks at $k=2\pi D$ (or $f=1/D$), and falls off again as k^{-2} at high frequency (Figure 3a).

Having found the effect of resetting on a single frequency, integration over k^* yields the total effect on the PSD of resetting an area of size D. Given an initial power spectrum with a steep slope at low frequencies, such as P_{build}, power is redistributed by resetting from the peak to lower frequencies, introducing a k^2 trend at the lowest frequencies (Figure 3).

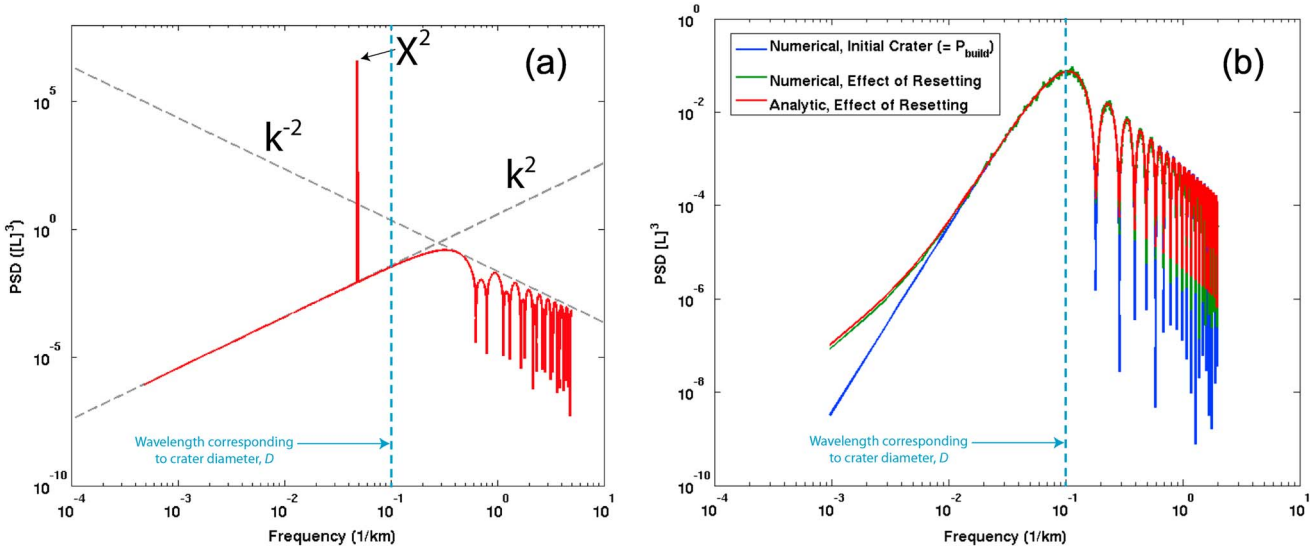

Figure 3. (a) PSD of a sinusoidal surface (of frequency k^*) on a domain of size $X = 1024$ km after an area $D = 5$ km has been reset to its own mean. Resetting transforms the initial PSD, a simple Delta function at $k = k^*$, such that the peak power diminishes, and power is added to low and high frequencies, where the PSD scales as k^2 and k^{-2}, respectively, peaking at $k \sim 2\pi/D$. (b) Effect on the PSD of resetting a surface containing a single crater. The numerical model is averaged over 100 instantiations, varying the location of the initial crater and the reset region. The analytic formulation sums the effect of resetting for each frequency (calculated from equation (7)), resulting in a redistribution of power from higher frequencies to lower frequencies, where the PSD scales as k^2.

The evolution of a 1-D terrain that accumulates craters of size D can thus be completely captured by iterating between resetting (equation (8)) and crater building (equation (6)), a procedure that can be written in matrix form:

$$P_{\text{final}} = \mathbf{M}P_{\text{initial}} + P_{\text{build}}. \tag{9}$$

M is the resetting matrix (each row of which is calculated from equation (8) for a different k^*) that acts on the initial PSD of the topography before P_{build} is added. This matrix representation is especially useful because the equation can be inverted to find the equilibrium power spectral density, where $P_{\text{final}} = P_{\text{initial}} = P_{\text{equil}}$:

$$P_{\text{equil}} = (\mathbf{I} - \mathbf{M})^{-1} P_{\text{build}}. \tag{10}$$

The analytic formulation presented here provides a consistent benchmark for the numerical model results under simplified conditions (1-D, self-similar craters of a single size, simple resetting algorithm), both for an evolving cratered terrain (Figure 4a) and a landscape in equilibrium (Figure 4b), illuminating the process effective at various scales. The first crater emplaced contributes the crater shape PSD, while subsequent craters increase the magnitude of the PSD everywhere and introduce the k^2 trend at low frequencies due to resetting the terrain. After approximately one covering time ($\sim X/D$ craters), the PSD reaches equilibrium at its peak frequency, corresponding to wavelengths of scale D, as well as all higher frequencies, and power in this frequency range ceases to evolve with time. As more craters are emplaced, equilibrium extends to larger scales according to the square root of the number of craters (a proxy for time in these simulations). It is important to note that while the area of a surface may be covered with craters, its power spectrum will continue to evolve well past a single covering time until equilibrium is achieved at all frequencies.

2.2. Synthetic PSDs

Because the equilibrium PSD for a given crater size D peaks at a unique frequency related to D, a procedure for combining craters of different sizes according to a given size-frequency distribution may be derived. The resulting PSD (referred to here as the "synthetic" PSD) can then be compared to the PSD derived from the numerical model, in which craters of different sizes are emplaced together on a domain.

The equilibrium PSD for single-size craters is characterized by a flat region at long wavelengths, a peak whose magnitude scales as D^3, and a k^{-2} tail at short wavelengths with peaks at integer multiples of D. Both the location and the magnitude of the primary peak vary with crater shape (h_r/d'), displaying different

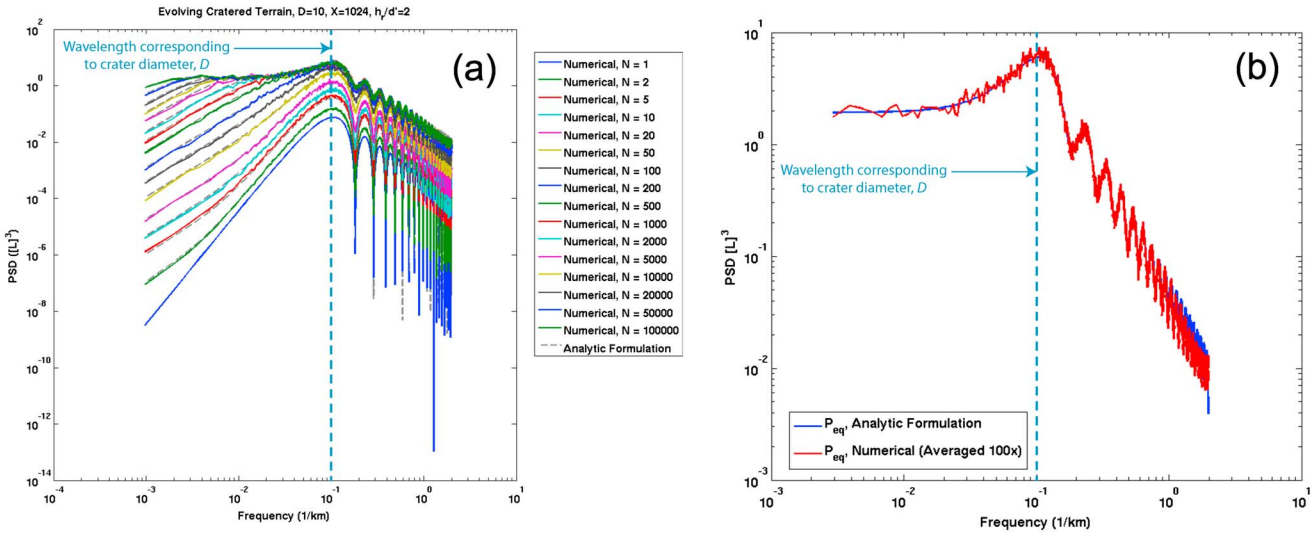

Figure 4. (a) Comparison of the numerical and analytic approaches to modeling the power spectral density of an evolving cratered terrain. All models are one-dimensional, with self-similar craters of diameter $D = 10$ km and no ejecta blanket ($h_r/d' = 2$). Dashed lines represent the analytic formulation, while colored lines show the numerical results averaged over 100 iterations each. After the first crater is emplaced, the PSD is exactly equal to P_{build}. As craters continue to accumulate, a k^2 trend is introduced at low frequencies, and the overall magnitude increases, clearly showing the alternating effects of resetting the surface and building new crater shapes. As the surface approaches equilibrium, the highest frequencies stabilize first, and the equilibrium PSD begins to take shape with the flat region shifting to lower frequencies. (b) Equilibrium PSD calculated by solving the matrix relation for resetting and building with craters of a single size $D = 10$ km (equation (9)). The analytic formulation agrees with the numerical model, which was averaged over 100 instantiations, each accumulating 10^5 craters on a domain of size $X = 1024$ km.

behaviors above and below $\gamma = 3$ (corresponding to $h_r/d' = 1$) (Figure 5a). For craters with little or no ejecta blanket, the peak in the PSD occurs at $f = 1/D$ and moves linearly to longer wavelengths as h_r/d' decreases (Figure 5a), according to

$$f_{max} = \begin{cases} \frac{1}{D} & \gamma \geq 3 \\ \frac{\gamma}{3D} & \gamma < 3. \end{cases} \quad (11)$$

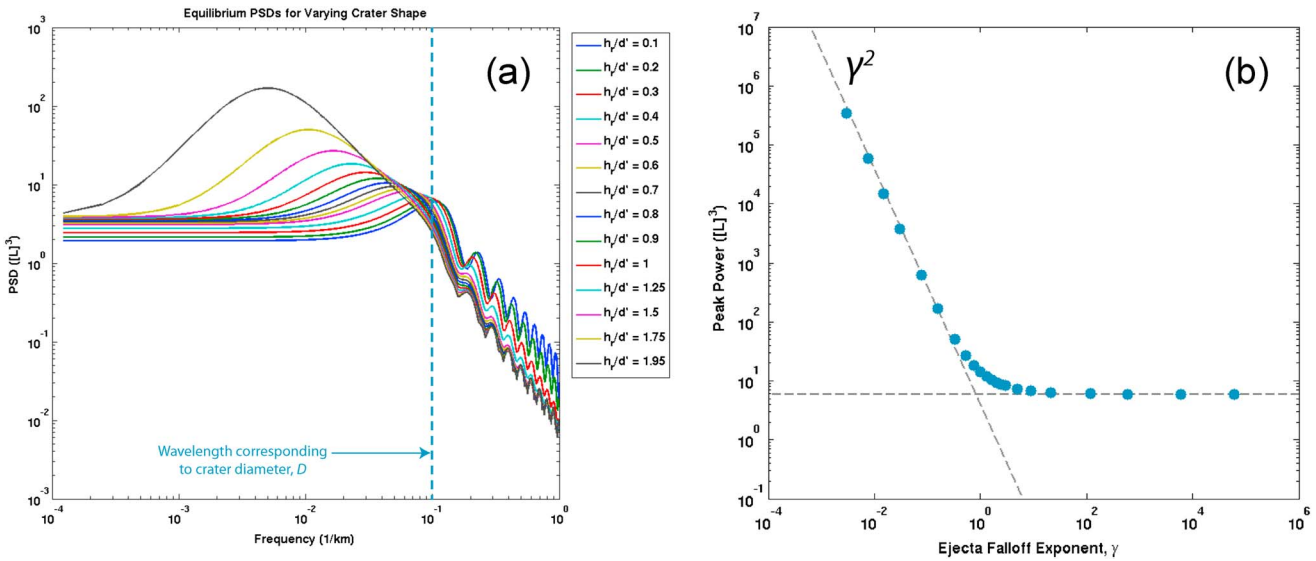

Figure 5. (a) Equilibrium PSDs for craters of size $D = 10$ km, consisting of a flat region at low frequencies, a peak whose location and magnitude depend on the crater shape parameters, and a high-frequency tail that falls off as k^{-2}. For high values of h_r/d' (high γ), the peak occurs at frequency $f = 1/D (k = 2\pi/D)$, and shifts to lower frequencies as the ejecta extent increases (as h_r/d' decreases). (b) In equilibrium, the peak of the PSD (for 1-D, single-size craters) is constant for high $\gamma (\gamma \geq 3,$ or $h_r/d' \geq 1)$ and scales as γ^2 for lower values. This corresponds to an increase in peak power for craters with extended ejecta blankets.

The magnitude of the peak is approximately constant for high values of γ and scales as γ^2 for smaller values (Figure 5b).

To first order, the power contributed by crater size D in equilibrium is dominated by the primary peak, which scales as D^3, as expected from equation (5) for self-similar craters and $f_D = 1$ for single-size craters. To approximate the equilibrium PSD of a terrain covered with craters of many sizes, we can add the individual single-size equilibrium PSDs in a prescribed proportion. This proportion depends on the frequency of occurrence (specified by the size-frequency power law exponent α) and the fraction of the surface, f_D, characterized by craters of that size. When large craters dominate the area (when $\alpha < L$, the dimensionality of the model), f_D is simply proportional to the area of the crater, D^L, because large craters erase everything smaller than themselves with a single covering. When small craters dominate the area, they must have time to diffuse topography at larger scales, and f_D is proportional to D^{L+2}. Using the latter relation, we expect the PSD to scale as

$$k^{-\beta} \sim D^{\beta} \sim D^3 D^{-\alpha} D^{L+2} = D^{L+5-\alpha}. \tag{12}$$

Comparing the result to our functional form for the PSD, $k^{-\beta}$, we find that in 1-D the PSD, β, obeys a simple relation: $\beta \sim 6 - \alpha$.

The slope of the power spectral density on a log-log plot against frequency, β, varies inversely with the size-frequency distribution exponent, α. As α increases, the number of small craters for every large crater also increases, producing more features on small scales and thus shallowing the PSD. We expect this tradeoff to occur at intermediate values of α, while in the high- and low-α limits, we expect β to become constant. For low α, the surface topography is dominated by craters of the largest size, $D_{\max}$, and the equilibrium PSD resembles the single-size PSD for $D_{\max}$. The peak therefore occurs at approximately $f \sim 1/D_{\max}$, which is near (but greater than) the minimum frequency set by the domain size, $1/X$. For all frequencies greater than $1/D_{\max}$, the PSD resembles the high-frequency tail of the single-size PSD for $D_{\max}$, which has a slope of $\sim k^{-2}$. Therefore, $\beta \sim 2$ in the low-α limit. For high α, the surface topography is dominated by the smallest craters, $D_{\min}$, and the equilibrium PSD resembles the single-size PSD for $D_{\min}$. The peak in the PSD occurs at approximately $f \sim 1/D_{\min}$, which is near (but less than) the maximum frequency set by the resolution of the model (the Nyquist frequency), and $\beta = 0$ for smaller frequencies. Thus, for a 1-D domain and to first order, we predict β to behave as follows

$$\beta = \begin{cases} 2 & \text{High } \alpha \\ 6 - \alpha & \text{Intermediate } \alpha \\ 0 & \text{Low } \alpha. \end{cases} \tag{13}$$

This prediction is tested in two ways: first, by synthetically combining the single-size PSDs according to the prescription derived above in equation (12) and second, by using the numerical model to emplace craters of different sizes together as a function of α. Figure 6 shows the results of both model types for 1-D, self-similar craters with no ejecta blanket ($h_r/d' = 2$) and values of α ranging from 0.25 to 8. For the numerical model, the PSD was averaged over many covering times. The power law exponent of the synthetic PSDs behaves as expected from equation (13): β remains relatively constant at $\beta \sim 2$ for low α and transitions to a constant at $\beta = 0$ for high α. Intermediate values of α generate PSDs that fit our expectation of $\beta \sim 6 - \alpha$.

The results of the numerical model show more structure than the first-order prediction summarized in equation (13), and this can be understood by considering in detail the processes of building and erosion of topographical features at every scale and the crater sizes that are most efficient at each of these processes. The range of size-frequency exponents, α, can thus be divided into several distinct regimes, which are marked by horizontal arrows in Figure 6. First, one may consider which crater size, for a given α, is most efficient at covering the area of the domain; the answer will depend on the footprint of the crater and its frequency of occurrence, and except for the special value of $\alpha = L$, either the smallest or the largest craters included in the model will dominate the area. At $\alpha = L$, all craters occupy an equal fraction of the total area of the domain. Which craters dominate the area, however, plays little role in the resulting behavior of β; this is determined by the interaction between building and erosion at every scale.

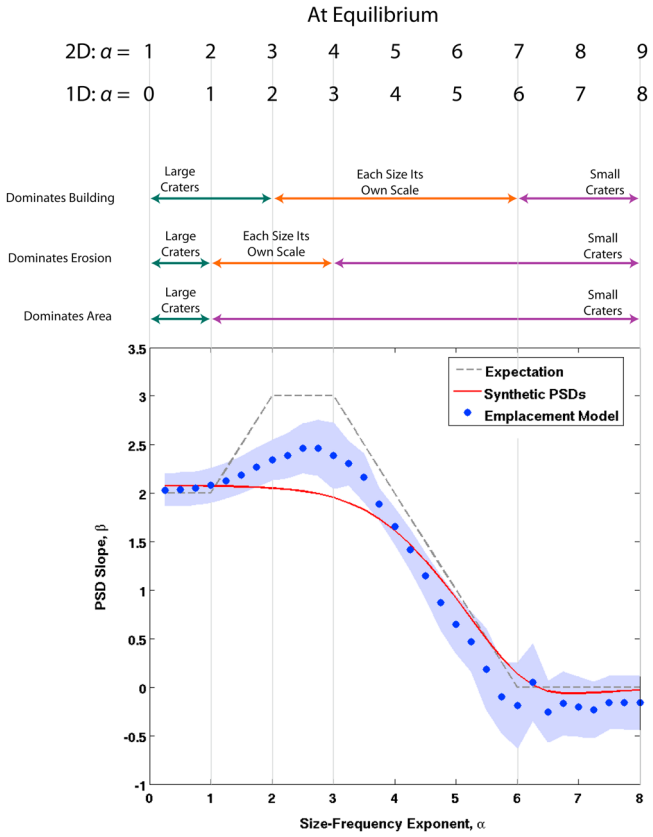

Figure 6. Power law exponent of the equilibrium PSD, β, comparing the numerical emplacement model, in which craters of different sizes are emplaced together according to a given size-frequency distribution, and the synthetic PSDs, which are a weighted sum of single-size equilibrium crater PSDs. The PSD is calculated from topography generated by the numerical model and averaged over many iterations once equilibrium conditions have been achieved (i.e., once the PSD ceases to evolve with the addition of more craters). The shaded region indicates 2σ error bars from the averaging and fitting the power law exponent.

To understand this interaction, we examine each significant range of α for building and erosion separately and then consider their joint effect. From Figure 4, it is clear that, for a given crater diameter, equilibrium is reached first at frequencies greater than or equal to the peak frequency ($f \sim 1/D$), and the PSD in this range goes as $\sim k^{-2}$. At all lower frequencies, the PSD is characterized by a k^2 trend before equilibrium is reached. For different values of α, the power at any given scale will be primarily contributed by either the smallest craters, the largest craters, or craters with diameters near that scale. In the first case, the smallest craters contribute a spectrum that goes as k^2 for all frequencies lower than $f \sim 1/D_{\min}$. Large craters, on the other hand, contribute a k^{-2} spectrum at all frequencies higher than $f \sim 1/D_{\max}$. In between, each crater of a given diameter D will contribute the most power to its own peak frequency, at which frequency the power scales as D^{3+L}, and the total power from all craters of size D scales with their number: $D^{3+L}D^{-\alpha}$. Comparing these contributions to the total PSD, we find the boundaries marked in Figure 6 for building. For a particular scale D, the largest craters and craters of size D will contribute equally to building when $\alpha = L + 1$, while the smallest craters and craters of size D will contribute equally when $\alpha = 5 + L$.

Just as with building, the erosion of features of a given scale will be dominated by either the largest craters, the smallest craters, or craters with diameters on that scale. The smallest craters diffuse their own scale (and smaller scales) in the time it takes them to cover the surface, but to erode larger craters, they must cover the surface many times. The time it takes to diffuse a crater of scale D' with craters of size $D (D \leq D')$ may be estimated as

$$t_{\text{diff}} \propto \left(\frac{D'}{D}\right)^2 D^{\alpha-L} \propto D^{\alpha-L-2}D'^2. \tag{14}$$

The diffusion time goes as D'^2, which is also reflected in Figure 4, as equilibrium spreads to lower frequencies at a rate proportional to the square root of the number of craters emplaced. Diffusion by the smallest craters thus contributes a k^{-2} spectrum to all larger scales. By contrast, large craters do not need to diffuse the scales smaller than themselves to erode them; they need only cover them. Once the surface has been covered with craters of the largest size, all smaller scales have also been eroded, and this process contributes a scale-independent spectrum, k^0. As with the building process, there is an intermediate range in which craters of each size dominate the erosion of their own scale, and this can be seen in equation (14) when $D = D'$. For this case, the diffusion time goes as $t_{\text{diff}} \propto D^{\alpha-L}$, and diffusion in this regime contributes a spectrum of $k^{L-\alpha}$. The boundaries of these erosion regimes are determined by comparing the spectra

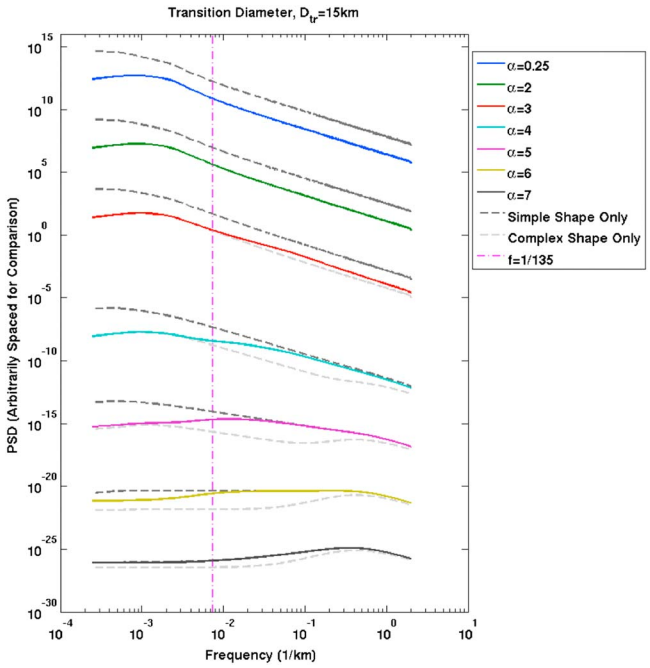

Figure 7. One-dimensional equilibrium PSDs for varying size-frequency distribution exponents, α, and a transition diameter, $D_{tr} = 15$km. Craters above D_{tr} are self-similar with shape parameters $h_r/d' = 0.5, \gamma = 1$ (complex craters); craters below D_{tr} are self-similar with shape parameters $h_r/d' = 0.2, \gamma = 1/3$ (simple craters). Dashed lines indicate model runs using only complex (light) or only simple (dark) crater shape parameters. For low $\alpha(< 3)$, equilibrium PSDs remain unaffected by the transition from simple to complex craters. For intermediate values of $\alpha(\sim 4-6)$, however, PSDs transition from matching the complex crater PSDs at low frequencies to matching the simple crater PSDs at high frequencies. This transition occurs first at $\alpha = 3$, where the extra power contributed by simple craters due to their shape (low h_r/d', extended ejecta) and high amplitude create a shoulder beginning at the peak frequency for the largest simple crater, $D = D_{tr} = 15$ km. As α increases, the PSD increases in magnitude at the high frequencies first, quickly coming to resemble the simple crater PSDs. At low frequencies, the PSD resembles the complex crater PSDs until the small craters overwhelm the large craters and the entire range resembles the simple crater PSD.

contributed by each class of craters. For a particular scale D, the largest craters and craters of size D will contribute equally to erosion when $\alpha = L$, while the smallest craters and craters of size D will contribute equally when $\alpha = L + 2$.

These building and erosion regimes, marked by arrows in Figure 6, can now be compared to determine the total effect on the behavior of β. For the steepest size-frequency distributions ($\alpha > L + 5$), the PSD is expected to scale as k^2 (from building) multiplied by k^{-2} (from erosion), yielding a value of $\beta = 0$. For α between $L + 2$ and $L + 5$, $k^{\alpha-L-3} \cdot k^{-2} = k^{\alpha-L-5}$ and $\beta = \alpha - L - 5$. The range of α between $L + 1$ and $L + 2$ is special in that craters of a given size dominate both the building and erosion of their own scale, and the resulting PSD power law exponent is independent of α : $k^{\alpha-L-3} \cdot k^{L-\alpha} = k^{-3}$. β is expected to be 3 in this range. For α between L and $L + 1$, $k^{-2} \cdot k^{L-\alpha}$ yields $\beta = \alpha - L + 2$, and for the smallest range of $\alpha < L$, $k^{-2} \cdot k^0$ predicts a constant value of $\beta = 2$, as equation (13) originally suggested. The numerical emplacement model reproduces this behavior in the power law exponent of the equilibrium PSD, with the exception that it fails to produce values of β greater than ~ 2.5, a circumstance that we believe would be improved (at significant computational expense) by further increasing the dynamic range of the model.

2.3. Effect of Crater Shape

The behavior described in Figure 6 applies in any models using self-similar craters, regardless of crater shape. This occurs because for a given shape parameter ratio h_r/d', the peak frequency is inversely proportional to D, preserving the scaling in equation (12). Realistic craters are not perfectly self-similar, but have shape parameters that scale with diameter. In addition to smooth changes in shape with increasing size, the transition diameter from simple to complex craters introduces an abrupt change, both in crater shape and in rim-to-floor depth (which is equivalent to the amplitude of the feature). This transition scales with surface gravity, and occurs around $D = 15$ km on the Moon. Morphometric relations for fresh lunar impact craters are listed in Table 4.1 in *Heiken et al.* [1991], based on *Pike* [1977] and *Pike* [1974]. Simple craters have a nearly constant shape parameter ratio of $h_r/d' \sim 0.23$, while complex craters span a range of values from $h_r/d' \sim 0.43$ to 0.67. Likewise, the rim-to-floor depths of simple craters scale linearly with their diameters, with a depth-to-diameter ratio of $d \sim 0.2$, and this observation is consistent with recent investigations based on LOLA topography data [*Talpe et al.*, 2012; *Fassett and Thomson*, 2014]. Simple crater shapes are thus approximately self-similar. Complex craters, by contrast, have lower amplitudes for their size, and this amplitude decreases with increasing diameter. The abrupt change in these two quantities—crater shape/ejecta extent and amplitude—at the transition diameter provides expectations for particular changes

Table 1. Morphometric Relations for Lunar Craters, From *Heiken et al.* [1991], Based on Measurements From *Pike* [1974] and *Pike* [1977]

	Rim Height (for D in km)	Rim-to-Floor Depth (for D in km)
Simple craters	$h_{rD} = 0.036D^{1.014}$ ($D < 15$ km)	$dD = 0.196D^{1.010}$ ($D < 15$ km)
Complex craters	$h_{rD} = 0.236D^{0.399}$ ($15 < D < 375$ km)	$dD = 1.044D^{0.301}$ ($12 < D < 275$ km)

in the shape of the PSD. Simple craters add more power relative to their diameters than complex craters, and they add this power to lower frequencies according to equation (11).

In one test, using self-similar craters with an abrupt transition at $D_{tr} = 15$ km from $h_r/d' = 0.2$ to 0.5 (corresponding to $\gamma = 1/3$ and $\gamma = 1$, respectively), synthetic PSDs for various values of α clearly reflect the change in crater shape (Figure 7). For comparison, the sample runs including only self-similar simple craters and only self-similar complex craters are included in Figure 7 as dashed dark and light gray lines, respectively. At low α, the equilibrium PSD resembles the corresponding complex-craters-only case, as the largest craters dominate. When $\alpha = 3$, the smallest craters start to contribute to the overall PSD, beginning at the peak frequency of the largest simple crater ($D_{tr} = 15, f_{peak} \sim \gamma/3D \sim 1/135 = 0.0074$) and extending to all higher frequencies. For intermediate α, between 4 and 6, the equilibrium PSD follows the complex crater curve at low frequencies and transitions to follow the simple crater curve at high frequencies. Above $\alpha \sim 6$, the PSD is equivalent to the simple-craters-only case. If, instead of the abrupt transition at $D_{tr} = 15$ km, the transition from simple to complex craters is smoothed out over a range of diameters near D_{tr} (e.g., from $D = 12$–18 km), the resulting PSDs are qualitatively similar to the abrupt transition case. Slight differences in the intermediate range of α's occur because the effect of the smallest craters is softened by the smoothed transition, and the larger craters dominate the total PSD shape to slightly higher frequencies.

Finally, we include the smooth power law scaling of crater shapes summarized in Table 1. Simple craters are nearly self-similar, and their behavior is well understood within the analysis described so far. Complex craters, however, are not self-similar; their rim-to-floor depth- and rim height-to-diameter ratios scale as $D^{0.301}$ and $D^{0.399}$, respectively (Table 1). This dependence on diameter leads to a modified expectation for the peak power scaling for individual crater sizes. According to equation (5), the power at the peak frequency goes as $P(f_{peak}) \sim H^2 D f_D$ (where the amplitude H is the rim-to-floor depth, dD). When the depth-to-diameter ratio d scales linearly with diameter and $f_{peak} \sim 1/D$, this peak power scales as D^3, as we have seen in our self-similar cratering models. In this case, however, $H \sim D^{0.301}$, and $f_{peak} \sim D^{-0.8}$ (according to equation (11)). Thus, the power at f_{peak} scales as $P(f_{peak}) \sim D^{0.602} D f_D \propto D^{1.602}$, from which we can calculate how the peak power scales with diameter:

$$P_{peak}(D) \sim \left(\frac{1}{D^{0.8}}\right)^{1.602} \sim D^{1.3}. \tag{15}$$

This scaling agrees with the results of the analytic model, and using equations (12) and (13), we can predict how the portion of the equilibrium PSD dominated by large craters behaves with varying size-frequency distribution. For intermediate values of $\alpha, \beta \sim 1.3 + 2 + L - \alpha = 4.3 - \alpha$. At frequencies dominated by small craters, the D^3 scaling for peak power still holds, and the original equations (12) and (13) are applicable. Thus, for one-dimensional versions of lunar-like craters, the equilibrium PSD has two slopes that evolve separately but predictably.

2.4. Two-Dimensional Emplacement Models

The equations developed thus far to describe the behavior of 1-D cratered terrains provide valuable predictions for the 2-D case as well. Here rather than calculating the two-dimensional Fourier transform to estimate the PSD, we calculate the 1-D PSD of each row and column of a 2-D model surface and compute the average to facilitate comparison with the LOLA along-track measurements. The 2-D model craters have an axisymmetric, parabolic cavity with a radial profile identical to that of their 1-D counterparts. The ejecta blanket function differs somewhat, however, because the condition for volume conservation becomes

$$\gamma = \frac{2h_r \left(d'/h_r\right)^{\frac{1}{2}}}{d' - h_r}. \tag{16}$$

Because the ejecta spreads out radially with distance from the crater, the maximum rim height (no ejecta) case occurs where $h_r/d' = 1$ and any given profile through the crater center is not itself area conserving. The peak power for an individual 2-D crater scales as D^5, the extra power of D arising from a second integral over the spatial parameter in equation (5). Real craters may exhibit ejecta bulk-up, resulting in an excess volume of ejecta compared to the excavated cavity [*Sharpton*, 2014]. Nevertheless, we do not expect this to affect the PSD of cratered terrains, as the peak power (determined to first order by the rim-to-floor depth) is unchanged. As before, it is possible to calculate Òsynthetic PSDsÓ of cratered terrains by adding the equilibrium PSDs of individual crater sizes in proportion to a given size-frequency distribution. The peak power of the equilibrium PSD scales as D^3 just as in the 1-D case, and the power is constant from the peak to lower frequencies. Equation (12) is used with a value of $L = 2$ to predict the slope of the PSD, β, as a function of the size-frequency distribution exponent, α:

$$\beta \sim L + 5 - \alpha = 7 - \alpha. \tag{17}$$

This behavior is consistent with the PSDs derived from the numerical emplacement model and is summarized in Figure 6. The power law exponent of the PSD for 1-D and 2-D domains is identical except for an offset of 1 in α.

2.5. Effect of Inheritance

Thus far, the resetting phase of crater emplacement has been modeled as simply as possible: the preexisting topography is surveyed and reset to its mean within half a diameter of the center of the new crater to be emplaced. This algorithm is convenient, as we have seen, in that it permits an analytical representation of the power spectral density evolving with multiple impacts, and it also takes into account the erasure of the initial terrain while providing a reasonable reference elevation upon which to superimpose the new crater topography. However, the physical processes taking place in an impact event, which our resetting phase only approximates, are poorly understood. Recent investigations of craters on steep slopes, such as those on Vesta [*Krohn et al.*, 2014], may contribute useful constraints to cratered terrain models, and other investigators have employed various algorithms to address this gap in our present understanding of the impact process. *Howard* [2007] introduces the inheritance parameter, I, which controls the degree to which preexisting topography is preserved during crater emplacement. Within the rim, the terrain is reset to a linear combination of a reference mean elevation, h_{ref}, and the initial topography, h_i, favoring the latter near the rim and the former in the center of the cavity. Between the center and the rim, the degree of resetting varies as a parabola scaled by I:

$$\Delta h_{reset} = (h_{ref} - h_i)\left[1 - I\left(\frac{2r}{D}\right)^2\right]. \tag{18}$$

This approach has the advantage that the edge produced at the rim by the resetting step is softened when I is greater than 0. This edge—equivalent to a step function in our simple resetting procedure—is responsible for the k^{-2} slope at high frequency in the equilibrium PSD for a single crater size, because the Fourier transform of a Heaviside function produces a slope of −1 in the frequency domain and the PSD is calculated from the square of the magnitude of the FFT. Hence, for terrains accumulating craters of many sizes, this choice of resetting algorithm has important consequences for the power spectral slope, which tends to level off at $\beta \sim 2$ when the size-frequency distribution is shallow (low α), as shown in equations (13) and (16). This occurs because the largest craters dominate the power, and the entire PSD comes to resemble the high-frequency tail of the single-size PSD for D_{max}.

To investigate how the choice of resetting algorithm affects the behavior of the PSD slope, we employed several variations of both our simple resetting procedure and the inheritance formula of *Howard* [2007] described above. We observed that algorithms producing a smoother terrain during the resetting phase (i.e., continuous at the rim, but not necessarily having a continuous first derivative) resulted in PSD slopes exceeding the value of $\beta \sim 2$ at low frequency. Figure 8 contains an example in which model runs use a variant of Howard's inheritance algorithm that is identical inside the crater rim but modified to be smoother outside to avoid unnecessary breaks in slope in the reset topography. The inheritance parameter, I, ranges here from 0 to 0.75, and the equilibrium PSDs for a size-frequency distribution with $\alpha = 1.5$ are plotted together, showing a clear steepening of the PSD at low frequency from $\beta \sim 2$ for $I = 0$ and $\beta \sim 3$ for $I = 0.75$. At high frequency, the slope is unchanged, indicating that the choice of resetting algorithm primarily affects long-wavelength topographic structures and is less important for small scales.

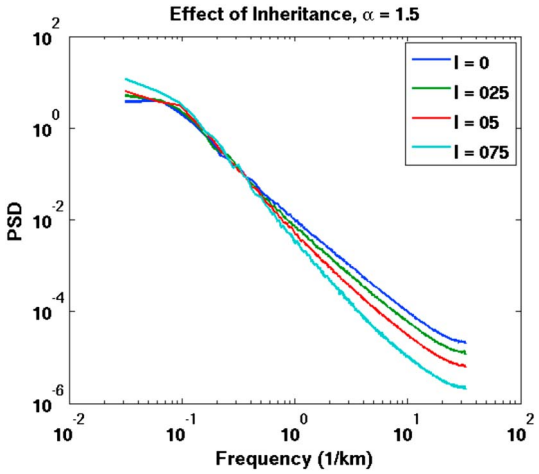

Figure 8. PSDs of cratered terrains with different values of *Howard*'s [2007] inheritance parameter, *I*. At high frequency, the slope is relatively unchanged, but at low frequency it steepens for smoother terrains generated using higher values of *I*.

3. Size-Frequency Distributions

Much work has been done to determine the size-frequency distribution (SFD) of craters in different areas of the Moon's surface [*Chapman and McKinnon*, 1986; *Hartmann and Gaskell*, 1997; *Neukum et al.*, 2001; *Ivanov et al.*, 2002] and to relate these observed crater size-frequency distributions to the population and flux of impactors that created them [*Hartmann and Gaskell*, 1997; *Richardson*, 2009]. These studies show that lunar craters do not follow a single power law over the entire range of crater sizes. Rather, the SFD is better approximated by a piecewise segmented power law or by a polynomial. The Hartmann production function (HPF) described in *Neukum et al.* [2001], formulated as the number of craters on typical mare surfaces, has three segments:

$$\begin{aligned} \log N_{\text{inc}} &= -2.616 - 3.82 \log D_{\text{L}} && D_{\text{L}} \le 1.41 \text{ km} \\ \log N_{\text{inc}} &= -2.920 - 1.80 \log D_{\text{L}} && 1.41 \text{ km} < D_{\text{L}} \le 64 \text{ km} \\ \log N_{\text{inc}} &= -2.198 - 2.20 \log D_{\text{L}} && D_{\text{L}} > 64 \text{ km}, \end{aligned} \tag{19}$$

where N_{inc} gives the number of craters in each $\sqrt{2}D$ diameter bin and D_{L} is the left boundary of each diameter bin. Small craters thus have a steeper size distribution than larger craters ($\alpha = 3.82$ versus $\alpha = 1.8$). This difference is significant because cratered terrains evolve quite differently for α above and below 2 (for a 2-D terrain), especially as they approach equilibrium, defined as the case where an incoming crater of size D will, on average, erase another crater of size D and the SFD of craters ceases to evolve with time [*Chapman and McKinnon*, 1986]. The analysis developed thus far for the dependence of the PSD power law exponent on α is therefore useful in understanding the behavior of observed lunar size-frequency distributions as well. As described in Figure 6, $\alpha = L$ (the dimensionality of the model or data domain) is a special size-frequency distribution in which craters of all sizes occupy equal areas of the domain. For values of α less than L, large craters cover more of the area than small craters, and they erase smaller craters than themselves simply by covering them. In this case, the equilibrium size-frequency distribution is not constant in time. Over time, small craters initially build up a size-frequency distribution that follows the original α, but they are erased by larger craters that reset much of the domain. On average, the initial power law slope α is preserved, but the instantaneous size-frequency slope oscillates around this value.

For values of $\alpha > L$, the area is dominated by small craters. If craters are assumed to be erased by covering only (as in the previous case), then the smallest craters, of size D_{min}, will erase all other crater sizes before they will have had time to come into equilibrium with themselves. Thus, the observed size-frequency distribution will have the same slope as the production function, α. However, as shown in Figure 6 and equation (14), diffusion is the dominant process of erosion for $\alpha > L$, and for $L < \alpha \le L + 2$, each crater size is responsible for the erosion of features on its own scale. In this case, crater rims are not destroyed in one covering, and all crater sizes have the opportunity to reach equilibrium with respect to their own size class. As *Soderblom* [1970] demonstrated analytically, the equilibrium size-frequency distribution of craters in this case is independent of α, following a power law slope of L. Starting from a flat plane, therefore, the size-frequency distribution will initially retain the production function power law slope α as craters accumulate. The smallest craters will reach equilibrium first, and a kink appears in the SFD, which has a slope of L at small crater sizes and α at large crater sizes. With time, this kink migrates to larger diameters until the entire size range is in equilibrium. The crater diameter at which the kink occurs is therefore an indication of the age of the cratered surface [*Gault*, 1970; *Melosh*, 1989, Figure 10.5]. This case can be compared to the behavior of the PSD in the range of α between $L + 1$ and $L + 2$, where both the building and erosion

processes at a given scale are dominated by craters of that scale, and the resulting PSD power law exponent is constant at $\beta = 3$.

For higher values of $\alpha (> L + 2)$, the smallest craters dominate the diffusion of all other scales, and they erase all larger craters faster than they can come into equilibrium with themselves. The diffusion time, t_{diff} scales as D^2 (equation (14)), such that larger craters take longer to erase in proportion to their area. The equilibrium size-frequency distribution of observed craters in this range of α is therefore proportional to $D^{2-\alpha}$. Thus, the production function can be recovered even after equilibrium has been achieved at all scales. This result is significant in that it is traditionally assumed that the equilibrium size-frequency distribution follows D^{-L} for all values of $\alpha > L$, as in the previous case [*Melosh*, 1989; *Richardson*, 2009]. However, *Soderblom* [1970] notes that his analytical model breaks down at $\alpha = 4$ (for $L = 2$) once the smallest craters begin to dominate diffusion, consistent with the results presented here.

The small-crater branch of the HPF has a power law exponent of −3.82, falling in the range $L < \alpha \leq L + 2$. At any given time, a particular size of crater, D_{cov}, has had just enough time to cover the domain once, and D_{cov} first coincides with the smallest craters (of size D_{min} in the cratered terrain model, but effectively infinitesimal in the case of the Moon) and subsequently moves to larger diameters with time. Given the coefficient in equation (19), D_{cov} can be calculated by comparing the segmented lunar size-frequency distribution to D^{-L}, which represents the maximum observable number of craters of that size. In the last ~3.5 Gyr (over the average age of the maria), the frequency of craters on the Moon in each $\sqrt{2}$ size bin goes as $10^{-2.616}D^{-3.82}$ (equation (19)). Multiplying by the area of each crater $\left(\frac{\pi}{4}D^2\right)$ and setting the result to 1 yields an estimate of the maximum crater size that has completely covered the surface:

$$10^{-2.616}D_{cov}^{-3.82}\frac{\pi}{4}D_{cov}^2 = 1. \tag{20}$$

For small craters, $D_{cov} = 32$ m. All craters smaller than this have also covered the entire surface at least once since the emplacement of the maria, but larger craters have not. This simple calculation is roughly consistent with crater counts down to smaller diameters than those included in the HPF, which indicate a cumulative size-frequency distribution (CSFD) slope of −2 for craters less than 100 m in diameter [*Shoemaker et al.*, 1970; *Soderblom*, 1970; *Hartmann*, 1985; *Namiki and Honda*, 2003]. As discussed in section 2.2, a single covering is not sufficient to bring a given crater size into equilibrium, as the −2 slope of the CSFD suggests, and equation (20) neglects effects of ejecta extent and random crater placement. Nevertheless, as a rough calculation, it provides an order of magnitude estimate of the scale at which a change in behavior is expected, and this scale is consistent with crater counts.

The models presented here emplace craters according to a simple power law production function, governed by a single value of α over the entire size range considered, in order to investigate the fundamental relationship between α and the resulting PSD slope. This production function is most relevant to the scenario in which different impactor populations are responsible for generating the separate branches of the CSFD. If the lunar production function is a broken power law like the HPF, with a steep $(\alpha > 2)$ branch at small sizes and a shallow $(\alpha < 2)$ branch at large sizes, larger craters will stochastically reset fields of smaller craters, so that the small-crater population will continue to reflect the production function at these scales [*Chapman and McKinnon*, 1986; *Melosh*, 1989; *Richardson*, 2009]. The power spectrum theory for cratering developed in previous sections predicts that, given a concave-up production function, the PSD will be dominated by the large-crater spectral signature, even at small scales. The high-frequency tail of the largest craters' PSD contributes more power at these frequencies than the peaks of the smallest craters' spectra, even though there are more of them. Thus, for a broken power law production function, we would expect the large-crater branch to dominate the overall PSD. However, more detailed modeling with complex production functions is needed to fully address this scenario.

4. Model Comparisons With Lunar Topography

The Lunar Orbiter Laser Altimeter (LOLA) is a multibeam laser altimeter carried on the Lunar Reconnaissance Orbiter that has collected over 6.3 billion measurements of lunar surface height since 2009 [*Barker et al.*, 2014]. Along-track measurements with a vertical precision of ~10 cm and accuracy of ~1 m are spaced approximately 57 m apart [*Smith et al.*, 2010a], and this high density provides an ideal opportunity to determine the power spectral density of lunar topography and compare the result to the PSDs generated using our cratered terrain model.

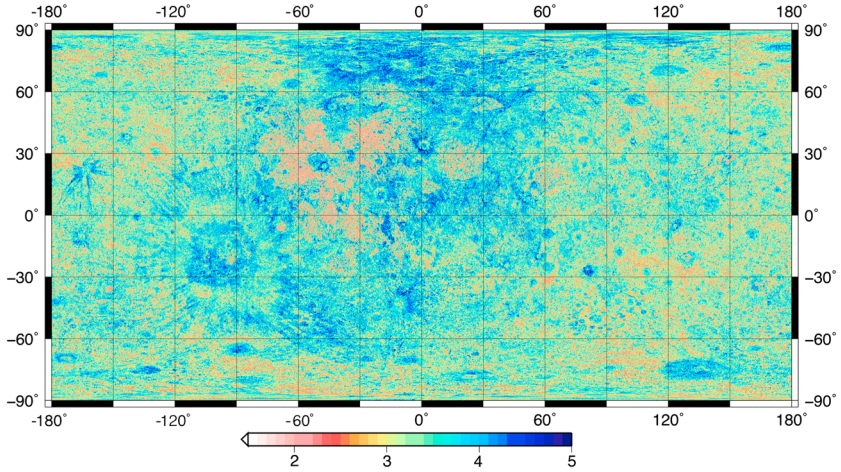

Figure 9. PSD slope (β) estimated for scales in the range of ~115 m to 1 km in overlapping windows of 1° (~30 km), spaced 0.1° (~3 km) apart.

The data were downloaded from the Planetary Data System, having been processed by the LOLA instrument team to remove anomalous data points (due to instrumental effects). Points were then binned along track in overlapping windows, and interpolated to a constant spacing. Windows with many consecutive missing points were excluded from the analysis to avoid introducing artifacts in the PSD. After de-meaning and detrending the profiles, the PSD was estimated within each window using the same multitaper algorithm as previously described, using four standard filters to accommodate the nonperiodic nature of the profiles. The choice of window size is important in measuring the power spectral slope, and after considering a wide range window sizes, we found the rule described in section 3.2.3 in *Shepard et al.* [2001] pertaining to Hurst exponent estimations to be applicable here as well. Measuring the PSD slope over a given range of spatial scales (inverse frequency) requires that the topographic profile length (window size) be no less than 10 times the maximum scale considered [*Shepard et al.*, 2001].

We use a least squares linear fit to measure the log-log slope of the PSD in two frequency ranges: the first samples topographic scales ranging from the smallest scale accessible with the LOLA data (twice the shot spacing, or roughly 115 m) to 1 km, and the second captures scales ranging from 1 to 6 km. Figures 9 and 10 contain maps of the PSD slope in each of these frequency ranges. The small-scale PSD slope (Figure 9) was calculated in 1° (~30 km) windows, while the few kilometer-scale PSD slope (Figure 10) used 3° (~90 km) windows. In both cases the windows were spaced 0.1° (~3 km) apart.

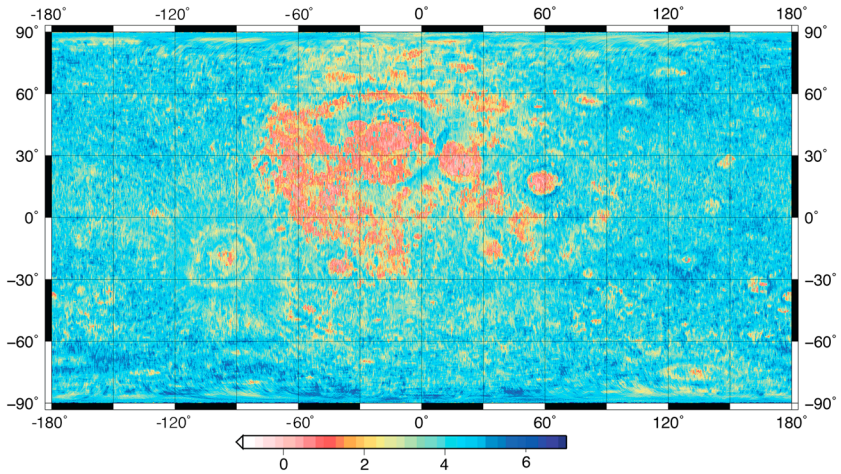

Figure 10. PSD slope (β) estimated for scales in the range of ~1 to 6 km in overlapping windows of 3° (~90 km), spaced 0.1° (~3 km) apart.

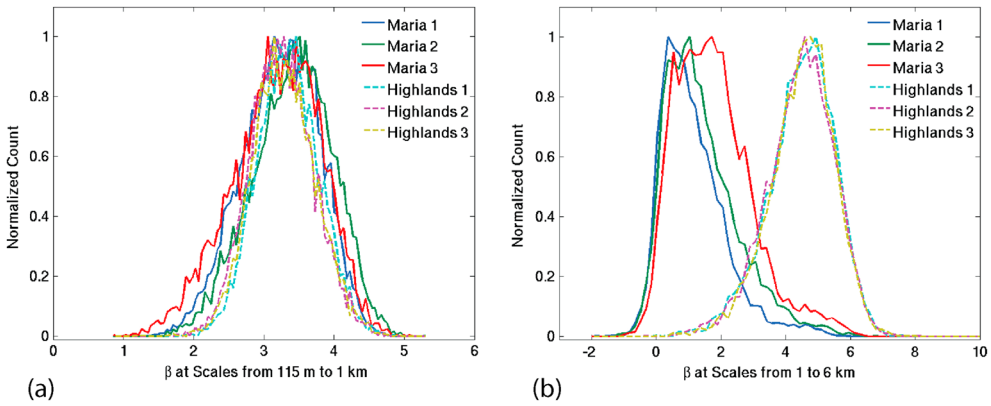

Figure 11. (a) PSD slope (β) histograms for selected areas in the maria (solid lines) and highlands (dashed lines), for scales between ~115 m and 1 km (corresponding to Figure 9). Latitude and longitude ranges for the selected regions are listed in Table 2. The spectral slope distributions overlap significantly, as would be expected if roughness features at this scale are controlled by the globally uniform process of regolith generation and modification. (b) PSD slope (β) histograms for scales between ~1 km and 6 km (corresponding to Figure 10). The distributions are distinct, with values of β falling primarily around 1 in the maria, while highlands values are much higher, with a peak around $\beta \sim 4.5$. The stark contrast between mare and highland regions is consistent with other roughness measurements that indicate a transition in the character of lunar roughness above and below approximately kilometer scales [*Rosenburg et al.*, 2011; *Kreslavsky et al.*, 2013]. Histograms are normalized by their maximum value to allow direct comparison of the distributions.

At small scales (~115 m to 1 km, Figure 9), $\beta \sim 3$ in the heavily cratered highlands, in reasonable agreement with the model for a value of $\alpha \sim 3.82$ (equation (19)) and when taking into account the effects of inheritance on resetting the terrain. This agreement supports the idea that cratering equilibrium has been reached at subkilometer scales. The boundary between the maria and the highlands is indistinct, indicating that at these scales (~115 m to 1 km) the regions are comparably rough, a result that agrees with those of other recent studies of lunar surface roughness [*Rosenburg et al.*, 2011; *Kreslavsky et al.*, 2013]. *Kreslavsky et al.* [2013] attribute this observation to the globally isotropic processes of regolith accumulation and modification, which produce and support roughness features on hectometer scales. This effect can also be seen in Figure 11a, which contains PSD slope (β) histograms for selected regions in the maria and highlands (2). Regions with significantly steeper PSD slopes ($\beta > 3$) occur in the floors of some large craters, where the topography is dominated by central peaks, rim terraces, and slump deposits on kilometer scales, a lengthscale that corresponds to the minimum frequency in the range sampled here. The most obvious example can be found in the floor of the crater Humboldt (27.2°S, 80.9°E), which is dominated by a complex rille network and range of central peaks (Figure 12). Similarly, the ring structure of Orientale Basin has a generally steeper PSD slope than the surrounding ejecta blanket, most likely due to prominent kilometer-scale topographical features. These types of features (rille networks, basin rings, etc.) are not captured in the model, and it is therefore not unexpected that they would deviate from the expected value of β.

Crater ray systems are also easily discernible as regions of higher β (appearing blue in Figure 9), suggesting that while they are not prominent in the raw elevation data, they do contain a unique topographical signature. In this case, it is likely that the rays have removed roughness at small scales relative to large ones (in this case, 115 m versus 1 km), producing a power spectral density profile that is depressed at the high-frequency end, and thus steeper than in the surrounding terrain. This steepening of the PSD may also be due in part to kilometer-scale chains of secondary craters which add power to the larger scales considered. *Rosenburg et al.* [2011] found a similar result in their differential slope analysis, showing

Table 2. Selected Regions in the Maria and Highlands for Spectral Slope β Histograms Shown in Figure 11

	Latitude	Longitude
Maria 1	22°N–32°N	12°E–22°E
Maria 2	30°N–40°N	7°W–17°W
Maria 3	30°N–40°N	60°W–70°W
Highlands 1	2°N–12°N	169°W–179°W
Highlands 2	45°N–55°N	95°W–105°W
Highlands 3	2°N–12°N	95°E–105°E

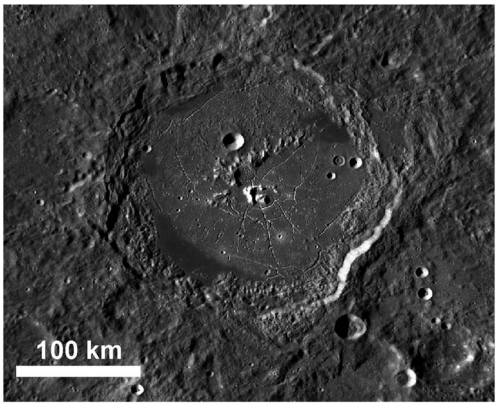

Figure 12. Lunar crater Humboldt, shown in the LROC Wide Angle Camera (WAC) mosaic (resolution of 100 m/pixel), in an orthographic projection centered at 27°S, 81°E.

that crater ray systems are more smooth at the shortest scales accessible with LOLA (~57 m) relative to kilometer scales than the rest of the highlands, while *Kreslavsky et al.* [2013] observed a similar effect using a related roughness measure, the curvature of topographic profiles. Prominent ray systems belong to Tycho (43.31°S, 11.36°W), Jackson (22.4°N, 163.1°W), and Ohm(18.4°S, 113.5°W), the youngest craters of their size [*Kreslavsky et al.*, 2013; *Hiesinger et al.*, 2012; *van der Bogert et al.*, 2010], as well as Aristillus (33.9°N, 1.2°E), Vavilov (0.8°S, 137.9°W), and Aristarchus (33.9°N, 1.2°E). As opposed to the age progression in topographic curvature noted by *Kreslavsky et al.* [2013], no clear correlation of the value of β with the age of rayed craters is evident. However, the slope of the PSD is not directly comparable to their surface roughness measure, which (for these features) looks at the 115 m scale only, the lower limit of the PSD range shown here.

Several localized areas of relatively shallow PSD slope ($\beta \sim 2-2.5$) occur in the interiors of the large mare-filled basins and as halos around prominent impact craters in the lunar highlands. A smaller value of β indicates a relatively greater contribution to the PSD from smaller scales compared to larger ones. In these cases, several factors may be at play. In the maria, crater saturation has likely not taken place for craters larger than approximately $D \sim 100$ m [*Richardson*, 2009], and there may be places that have not been completely covered by craters since the emplacement of the mare basalts. The absence of crater overlap in this case, together with the limited time available since the surface was reset for larger craters to accumulate, may have resulted in a dearth of topographical features contributing to the low-frequency end of our frequency range and a consequent shallowing of the PSD slope. The regions of relatively low β surrounding prominent craters may be due not to an absence of power at large scales, but rather an addition of small scale features, especially rim terraces and blocky ejecta deposits. Haloes of this nature were also noted by *Kreslavsky et al.* [2013] at the 1 km scale, where ejecta transitions from proximally smooth to distally rough. Similar cases, where small-scale roughness is low near the crater rim (with values of $\beta \sim 4$) and becomes relatively high further away ($\beta \sim 2$), include the farside craters Fermi (19.3°S, 122.6°E) and Kovalevskaya (30.8°N, 129.6°W).

Figure 10 shows the PSD slope measured at somewhat larger scales, spanning the range from 1 to 6 km, and Figure 11b contains PSD slope histograms within selected mare and highland regions for this frequency range. Whereas the maria and highlands were not easily distinguishable in the small scale PSD shown in Figure 9, here they are quite distinct, with the maria displaying much lower PSD slopes ($\beta \sim 1$) than the highlands ($\beta \sim 3.5-5$). The relatively low values of β in the mare regions reflects the absence of features at the few kilometers scale, aside from prominent wrinkle ridges and decameter-scale craters, which appear as isolated spots of higher β. By contrast, the PSD slope in highland regions is higher than expected from the model, suggesting that processes not captured in the cratering dynamics modeled here may act at these scales. The highest values of β at these scales tend to occur in places with relatively low β at the smaller scales measured, and the two values may be influencing each other.

This stark contrast between the maria and the highlands is characteristic of lunar roughness above and below approximately kilometer scales. *Rosenburg et al.* [2011] noted that the Hurst exponent—a measure ranging from 0 to 1 that describes the scaling of surface slopes with horizontal baseline—transitions in the highlands from approximately 1 (indicating nearly self-similar behavior) at small scales to a smaller value of approximately 0.8, with the transition occurring near 1 km. Similarly, *Kreslavsky et al.* [2013] found a clear difference in the character of lunar surface roughness at hectometer and kilometer scales. This behavior is consistent with a transition between roughness regimes controlled by competing surface processes acting at different scales [*Turcotte*, 1997; *Perron et al.*, 2008], including the accumulation of regolith through impact gardening processes, the global erasure of roughness features by seismic shaking during large

basin-forming impacts, and early tectonic and volcanic events that formed the prominent mare plains and wrinkle ridges [*Rosenburg et al.*, 2011; *Kreslavsky et al.*, 2013; *Richardson*, 2009].

5. Conclusions

We have developed a model capable of tracking the evolution of a cratered terrain from an initially flat plane through saturation equilibrium. Having benchmarked the model against an analytical solution in 1-D, we conclude that the power spectral density of a surface created only by impacts can be predicted from the size-frequency distribution of craters emplaced. The analytical approach reveals the principles governing the surface evolution, and in comparing the results of the model to calculations of the PSD along LOLA transects, we find good agreement at small scales down to 115 m. Exceptions to the model occur in places where competing geomorphological processes, such as tectonics, dominate, or when crater saturation has not yet been achieved.

The model predicts behaviors for the PSD slope β at a range of size-frequency distribution exponents (α), not all of which can be tested with the lunar topography. Our results suggest that the power spectral density and observed size-frequency distribution of a cratered terrain both provide clues to the production size-frequency distribution of craters. Whereas the observed SFD is expected to be constant at equilibrium within a range of α between L and $L + 2$ ($2 \leq \alpha < 4$ for the Moon), the slope of the PSD, β, is only constant over part of this range ($L + 1 \leq \alpha < L + 2$). Thus, these two measures are complementary in the sense that they each provide information as to the production function. Furthermore, we affirm the suggestion first made by *Soderblom* [1970] that above a value of $\alpha = L + 2$, the erasure of craters is dominated by diffusion by the smallest crater sizes, and the production function can again be obtained from the observed SFD of craters. Impact cratering is a dominant agent of surface modification in our solar system, and it is hoped that the conclusions drawn here can be applied to many planetary surfaces, including those of Mercury, Mars, and the outer planets' satellites.

Acknowledgments

Topography data collected by the Lunar Orbiter Laser Altimeter (LOLA) are available at the LOLA/LRORS PDS Data Node at http://imbrium.mit.edu. The authors acknowledge support from the Lunar Reconnaissance Orbiter project, NASA LOLA grant NNX15AB23G, the Weizmann Minerva Center, I-Core, ISA, ISF, and the Packard Fellowship programs.

References

Barker, M., et al. (2014), Merging digital elevation models from the lunar orbiter laser altimeter and Kaguya terrain camera, in *Lunar and Planetary Institute Science Conference Abstracts*, vol. 45, p. 1635, Lunar and Planet. Inst., The Woodlands, Tex.

Chapman, C. R., and W. B. McKinnon (1986), Cratering of planetary satellites, in *IAU Colloq. 77: Some Background about Satellites*, vol. 1, pp. 492–580, Univ. of Ariz. Press, Tuczon.

Fassett, C. I., and B. J. Thomson (2014), Crater degradation on the lunar maria: Topographic diffusion and the rate of erosion on the Moon, *J. Geophys. Res. Planets*, *119*, 2255–2271, doi:10.1002/2014JE004698.

Gault, D. E. (1970), Saturation and equilibrium conditions for impact cratering on the lunar surface: Criteria and implications, *Radio Sci.*, *5*(2), 273–291.

Hartmann, W. K. (1985), Impact experiments: 1. Ejecta velocity distributions and related results from regolith targets, *Icarus*, *63*(1), 69–98.

Hartmann, W. K., and R. W. Gaskell (1997), Planetary cratering 2: Studies of saturation equilibrium, *Meteorit. Planet. Sci.*, *32*(1), 109–121.

Heiken, G., D. Vaniman, and B. M. French (1991), *Lunar Sourcebook: A User's Guide to the Moon*, CUP Archive, New York.

Hiesinger, H., R. Jaumann, G. Neukum, and J. W. Head (2012), Ages of mare basalts on the lunar nearside, *J. Geophys. Res.*, *105*(E12), 29,239–29,275.

Howard, A. D. (2007), Simulating the development of Martian highland landscapes through the interaction of impact cratering, fluvial erosion, and variable hydrologic forcing, *Geomorphology*, *91*(3), 332–363.

Ivanov, B., G. Neukum, W. Bottke, and W. Hartmann (2002), The comparison of size-frequency distributions of impact craters and asteroids and the planetary cratering rate, *Asteroids III*, *1*, 89–101.

Kreslavsky, M. A., J. W. Head, G. A. Neumann, M. A. Rosenburg, O. Aharonson, D. E. Smith, and M. T. Zuber (2013), Lunar topographic roughness maps from Lunar Orbiter Laser Altimeter (LOLA) data: Scale dependence and correlation with geologic features and units, *Icarus*, *226*(1), 52–66.

Krohn, K., et al. (2014), Asymmetric craters on Vesta: Impact on sloping surfaces, *Planet. Space Sci.*, *103*, 36–56.

Melosh, H. J. (1989), *Impact Cratering: A Geologic Process, Research Supported by NASA*, Oxford Univ. Press, New York. (Oxford Monographs on Geology and Geophysics, No. 11), 1.

Namiki, N., and C. Honda (2003), Testing hypotheses for the origin of steep slope of lunar size-frequency distribution for small craters, *Earth Planets Space*, *55*(1), 39–52.

Neukum, G., B. A. Ivanov, and W. K. Hartmann (2001), Cratering records in the inner solar system in relation to the lunar reference system, *Space Sci. Rev.*, *96*(1–4), 55–86.

Perron, J. T., J. W. Kirchner, and W. E. Dietrich (2008), Spectral signatures of characteristic spatial scales and nonfractal structure in landscapes, *J. Geophys. Res.*, *113*, F04003, doi:10.1029/2007JF000866.

Pike, R. (1977), Apparent depth/apparent diameter relation for lunar craters, in *Lunar and Planetary Science Conference Proceedings*, vol. 8, pp. 3427–3436, Lunar and Planet. Inst., The Woodlands, Tex.

Pike, R. J. (1974), Depth/diameter relations of fresh lunar craters: Revision from spacecraft data, *Geophys. Res. Lett.*, *1*(7), 291–294.

Richardson, J. E. (2009), Cratering saturation and equilibrium: A new model looks at an old problem, *Icarus*, *204*(2), 697–715.

Richardson, J. E., H. J. Melosh, N. A. Artemeiva, and E. Pierazzo (2005), Impact cratering theory and modeling for the deep impact mission: From mission planning to data analysis, in *Deep Impact Mission: Looking Beneath the Surface of a Cometary Nucleus*, pp. 241–267, Springer, Dordrecht, Nethrlands.

Robbins, S. J., et al. (2014), The variability of crater identification among expert and community crater analysts, *Icarus*, *234*, 109–131.

Rosenburg, M., O. Aharonson, J. Head, M. Kreslavsky, E. Mazarico, G. Neumann, D. Smith, M. Torrence, and M. Zuber (2011), Global surface slopes and roughness of the Moon from the lunar orbiter laser altimeter, *J. Geophys. Res.*, *116*, E02001, doi:10.1029/2010JE003716.

Sharpton, V. L. (2014), Outcrops on lunar crater rims: Implications for rim construction mechanisms, ejecta volumes and excavation depths, *J. Geophys. Res. Planets*, *119*, 154–168, doi:10.1002/2013JE004523.

Shepard, M. K., B. A. Campbell, M. H. Bulmer, T. G. Farr, L. R. Gaddis, and J. J. Plaut (2001), The roughness of natural terrain: A planetary and remote sensing perspective, *J. Geophys. Res.*, *106*, 32,777–32,796, doi:10.1029/2000JE001429.

Shoemaker, E., M. Hait, G. Swann, D. Schleicher, D. Dahlem, G. Schaber, and R. Sutton (1970), Lunar regolith at tranquillity base, *Science*, *167*(3918), 452–455.

Smith, D. E., et al. (2010a), The lunar orbiter laser altimeter investigation on the lunar reconnaissance orbiter mission, *Space Sci. Rev.*, *150*, 209–241, doi:10.1007/s11214-009-9512-y.

Soderblom, L. A. (1970), A model for small-impact erosion applied to the lunar surface, *J. Geophys. Res.*, *75*(14), 2655–2661.

Talpe, M. J., M. T. Zuber, D. Yang, G. A. Neumann, S. C. Solomon, E. Mazarico, and F. Vilas (2012), Characterization of the morphometry of impact craters hosting polar deposits in Mercury's north polar region, *J. Geophys. Res.*, *117*, E00L13, doi:10.1029/2012JE004155.

Turcotte, D. L. (1997), *Fractals and Chaos in Geology and Geophysics*, Cambridge Univ. Press, New York.

van der Bogert, C. H., H. Hiesinger, A. S. McEwen, C. Dundas, V. Bray, M. S. Robinson, J. B. Plescia, D. Reiss, K. Klemm, and Lroc Team (2010), Discrepancies between crater size-frequency distributions on ejecta and impact melt pools at lunar craters: An effect of differing target properties?, in *Lunar and Planetary Science Conference, Lunar and Planetary Science Conference*, vol. 41, p. 2165, Lunar and Planet. Inst., The Woodlands, Tex.